JEM

Journal of Electron Microscopy **60(Supplement 1)**: S173–S188 (2011)
doi: 10.1093/jmicro/dfr049

60th Anniversary Issue: Physical

Grain boundary atomic structures and light-element visualization in ceramics: combination of Cs-corrected scanning transmission electron microscopy and first-principles calculations

Yuichi Ikuhara[1,2,3,*]

[1]Institute of Engineering Innovation, The University of Tokyo, Tokyo 113-8656, Japan, [2]Nanostructures Research Laboratory, Japan Fine Ceramic Center, Nagoya 456-8575, Japan and [3]WPI Research Center, Advanced Institute for Materials Research, Tohoku University, Sendai 980-8577, Japan
*To whom correspondence should be addressed. E-mail: ikuhara@sigma.t.u-tokyo.ac.jp

Abstract Grain boundaries and interfaces of crystals have peculiar electronic structures, caused by the disorder in periodicity, providing the functional properties, which cannot be observed in a perfect crystal. In the vicinity of the grain boundaries and interfaces, dopants or impurities are often segregated, and they play a crucial role in deciding the properties of a material. Spherical aberration (Cs)-corrected scanning transmission electron microscopy (STEM), allowing the formation of sub-angstrom-sized electron probes, can directly observe grain boundary-segregated dopants. On the other hand, ceramic materials are composed of light elements, and these light elements also play an important role in the properties of ceramic materials. Recently, annular bright-field (ABF)-STEM imaging has been proposed, which is now known to be a very powerful technique in producing images showing both light- and heavy-element columns simultaneously. In this review, the atomic structure determination of ceramic grain boundaries and direct observation of grain boundary-segregated dopants and light elements in ceramics were shown to combine with the theoretical calculations. Examples are demonstrated for well-defined grain boundaries in rare earth-doped Al_2O_3 and ZnO ceramics, CeO_2 and $SrTiO_3$ grain boundary, lithium battery materials and metal hydride, which were characterized by Cs-corrected high-angle annular dark-field and ABF-STEM. It is concluded that the combination of STEM characterization and first-principles calculation is very useful in interpreting the structural information and in understanding the origin of the properties in various ceramics.

Keywords ABF-STEM, grain boundary, ceramics, dopant, light element

Received 24 March 2011, accepted 16 June 2011

1. Introduction

The mechanical and electronic properties of ceramics are strongly influenced by the atomic structure of grain boundaries and interfaces [1–3]. On the other hand, grain boundaries and interface structures themselves are sensitive to the characteristics of grain boundaries. Therefore, it is important to investigate the relationship between grain boundary structure and its characteristics so that we can understand how grain boundary structure affects the intrinsic properties of ceramics. Doping impurities into ceramics is a useful means to control grain boundary properties.

The impurities often segregate along the grain boundary, changing the intrinsic properties. It has been well known that a small amount of rare earth doping improves the mechanical and functional properties of various ceramics [4]. The properties of ceramics, in which light elements are the main constituents, are also dependent on the atomic sites and distribution of the light elements in the microstructures. It is, therefore, required to directly observe light elements in ceramics to understand the origin of their functional properties.

So far, transmission electron microscopy (TEM), in particular, high-resolution electron microscopy (HRTEM), has been a useful technique for studying the atomic structure of grain boundaries and was used to investigate various types of grain boundaries in many types of ceramics. However, among recent nano-characterization technologies, there has been remarkable progress by scanning transmission electron microscopy (STEM) utilizing the spherical aberration (Cs) corrector [5]. This technique enables us not only to identify the atomic structures, but also to locate dopants segregated at grain boundaries and interfaces. An STEM image is formed by the scattered electrons in each probe position collected by the annular dark-field (ADF) detector at the bottom of the sample, displayed on the monitor in synchronism with the scanning probe [6–8]. An atomic resolution image can be obtained by focusing the electron probe down to below the atomic column interval. On the other hand, very recently, annular bright-field (ABF)-STEM imaging has successfully been used for imaging columns of both light and heavy elements simultaneously with a good signal-to-noise ratio [9–11]. This is a very promising technique because of its sensitivity to light elements and the robustness of the interpretation of direct images for a large range of sample thicknesses [10,11]. Using this imaging technique, light elements such as Li ions and even hydrogen atoms have been visualized successfully in real-space and real-time [12–16].

At the same time, first-principles and semi-empirical theoretical calculations have been developed to quantitatively interpret the images and spectra obtained by STEM. It is, therefore, very useful to use theoretical calculations based on the experimental data to understand the origin of the properties and to obtain a guideline for designing advanced ceramics. In this review, recent progress on grain boundary and light-element characterization by high-angle ADF (HAADF) and ABF-STEM for various ceramics is discussed. The atomic structures of coincidence site lattice (CSL) grain boundaries are consisted of various types of structural units, which often determine the macroscopic properties. In this study, the structural units formed in CeO_2 and $SrTiO_3$ grain boundaries are directly observed, and the stable structures are quantitatively discussed. In addition, grain boundaries have peculiar electronic structures, caused by the disorder in the structure units, providing the functional properties, which cannot be observed in a perfect crystal. In the vicinity of the grain boundaries, dopants or impurities are often segregated, and they play a crucial role in deciding the properties of a material. Here, the dopants segregated at the grain boundaries are directly characterized by STEM, and the role of the dopants on the properties is discussed from the results obtained by the theoretical calculations. On the other hand, ceramics are composed of light elements. For example, the properties of a lithium battery are strongly dependent on the behavior of lithium ions during the charge/discharge process. Since this behavior determines the stability, lifetime and reliability, direct visualization of a Li site is needed to understand the mechanism of the properties. In this study, ABF-STEM technique is demonstrated to directly observe Li and O ions in $LiCoO_2$ and $LiMn_2O_4$ battery materials, and also hydrogen columns in metal hydrides.

2. Scanning transmission electron microscopy

2.1 High-angle ADF-scanning transmission electron microscopy

STEM is a technique used for scanning a specimen by an electron probe, which is focused down to 1 nm or less on the sample. The STEM image is formed with the collected scattered electrons in each probe position by the ADF detector at the bottom of the sample on the monitor in synchronism with the scanning probe [6,7]. The atomic resolution image can be obtained by focusing the electron probe down to below the atomic column interval.

The advantages of this method are as follows: there is no inversion of the image contrast with the defocusing and the change in the sample thickness, and thus the positions of the atomic columns can be determined directly from the image. These excellent characteristics are very useful in determining the complicated atomic structures in the grain boundaries and interfaces. In addition, the intensity of the image obtained by detecting the electrons scattered to higher angles is known to correspond to about the square of the atomic number Z. The contrast of HAADF-STEM is therefore called 'Z-contrast' as well, making it possible to observe the element distribution at an atomic column level in the region where local composition is changed. Moreover, in recent years, by combining the STEM method with the Cs correction technology, drastic improvement in resolution has become possible. At present, with the STEM using the Cs corrector, the electron probe diameter of 1 Å or less has already been achieved [8]. Furthermore, since the intensity of the electron probe can be increased by the Cs correction technology, there are advantages that the S/N ratio of the STEM image will be increased and hence the image quality can also be improved drastically. The STEM method using the Cs corrector is thus expected as a powerful tool to characterize the atomic structures in grain boundaries and interfaces.

In the present experiments, STEM observations were performed using a Cs-corrected STEM (JEM-2100F/ARM-200F, JEOL, Co., Tokyo, Japan) operated at 200 kV and equipped with a spherical aberration corrector (CEOS GmbH, Heidelberg, Germany), which provided a minimum probe <1 Å in diameter.

2.2 Annular bright-field-scanning transmission electron microscopy

It has been proposed that an annular detector located within the bright-field region enables the simultaneous imaging of light and heavy elements in STEM [9–11]. The geometry of the ABF imaging mode is shown in Fig. 1a. In the case, $\alpha = \beta_2$, the contrast of ABF-STEM image seems to be good. The optimum inner angle is not clearly determined, though we typically find the upper half of the outer angle to be suitable [10,11]. Figure 1b–e shows simultaneous ADF and ABF images of TiO_2 [001] and $SrTiO_3$ [110]. The ADF images show the atomic locations as bright spots, whereas the ABF images have the absorptive form with atomic column locations indicated by dark spots. It can be seen that while the oxygen locations are at best vague in the TiO_2 ADF image and basically invisible in the $SrTiO_3$ ADF image, they are clearly visible in the ABF images.

Findlay *et al.* [10,11] reported that ABF imaging not only allows for the simultaneous imaging of light- and heavy-atom columns, but also allows for robust interpretation over a wide range of specimen

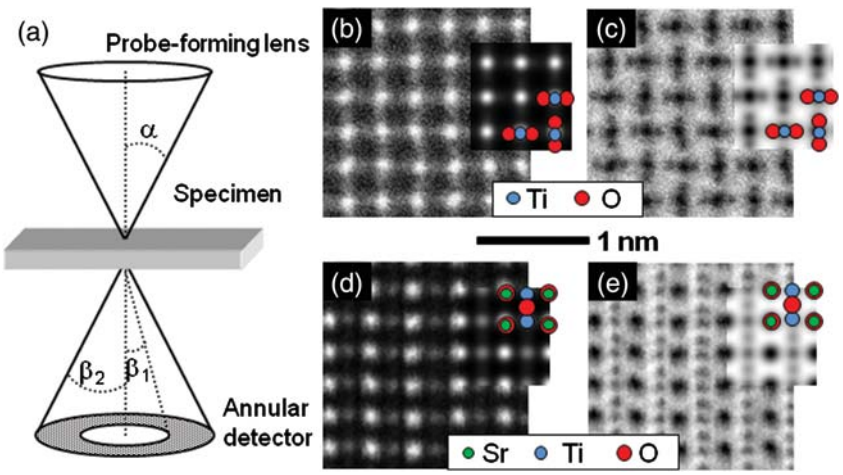

Fig. 1. (a) Schematic of the ABF imaging geometry. The probe-forming aperture semi-angle is denoted by α. The detector inner and outer angles are given by β_1 and β_2. (b) HAADF and (c) ABF images of TiO_2 [001], and (d) HAADF and (e) ABF images of $SrTiO_3$ [110]. All images were recorded on the JEOL ARM-200F at 200 keV, with $\alpha = 22$ mrad. For HAADF, $\beta_1 = 90$ mrad and $\beta_2 = 170$ mrad. For ABF, $\beta_1 = 11$ mrad and $\beta_2 = 22$ mrad. Simulations (convolved with a Gaussian of half-width-half-maximum 0.4 Å to approximately account for finite source size effects) and projected structures are given in the insets.

thicknesses. The ADF image displays the robustness with respect to thickness that has made it such a successful experimental technique. In addition, in the ABF image, we see that the location of all columns is clearly visible over the full range of thickness values up to ~60 nm, albeit for a relatively narrow (compared with ADF) range of defocus values. It has been shown that the ABF-STEM imaging offers the possibility of directly observing very light-element atoms such as Li atoms [12–14] and even hydrogen atoms [15,16] in bulk materials.

3. CSL grain boundary in ceramics

3.1 Atomic structures of a CeO_2 grain boundary

Among the oxides, fluorite-structured ceria (CeO_2) and ceria-based compounds are attractive materials for electrolytes in solid oxide fuel cells and catalysis because of their unique redox and transport properties. Here, the atomic structure of a (210)Σ5 CeO_2 grain boundary was studied using STEM with HAADF and ABF detectors. We selected a (210)Σ5 grain boundary with a common tilt axis of [001] as a model grain boundary. The aim of this study was to determine both the cation and oxygen sublattices of this CeO_2 grain boundary, including the oxygen non-stoichiometry so as to reveal the role of the oxygen vacancies on the grain boundary atomic structure.

Figure 2a and c displays typical HAADF and ABF images for the (210)Σ5 CeO_2 grain boundary viewed along [001] direction, respectively [17]. In the HAADF image, the bright spots correspond to the Ce column locations, while the O columns surrounded by four Ce columns are not evident because the atomic number Z of oxygen is too small. On the other hand, oxygen columns can directly be identified in the ABF image, in which the columns appear with dark contrast, as indicated by the arrows in Fig. 2c and d. It is found that the atomic columns of Ce are observed even in the grain boundary core region, and the grain boundary is made of repeating structural units, which are marked by quadrilaterals in Fig. 2a and c. Where the sample is thin and two crystals are well orientated, we generally observe such structural units repeating over stretches of interface 10–20 nm in length with steps in between. In this region, the atomic structure is reproducible, and we characterized this structure for further calculations.

In order to determine the atomic structure of the observed CeO_2 grain boundary, the grain boundary structure was first modeled using a static lattice calculation with the GULP program code [18,19]. We used a rectangular supercell that contained 240 atoms and two equivalent grain boundaries. The resultant stable structures were optimized using VASP code [20]. The stable grain boundary structures thus obtained are shown in the inset in Fig. 2a and c for the non-stoichiometric grain boundary. Due to the presence of oxygen vacancies, the electrostatic

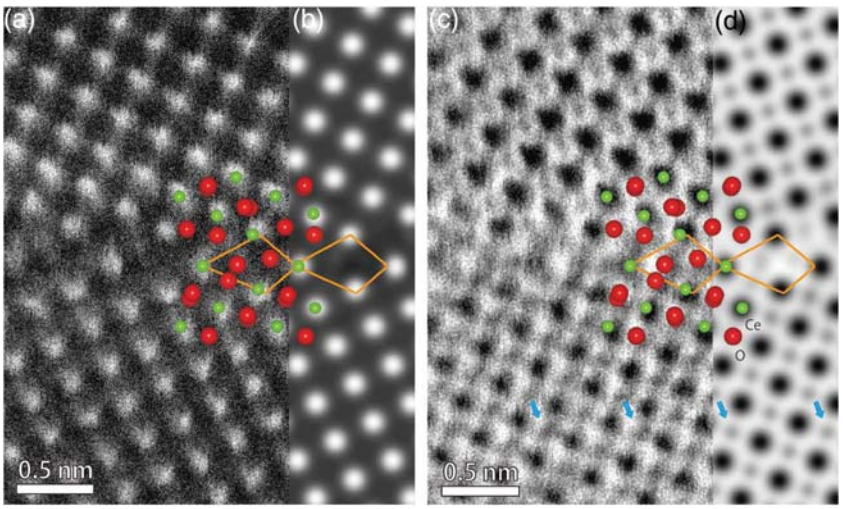

Fig. 2. (a) HAADF and (c) ABF images of a [001](210)Σ5 grain boundary in a CeO_2 thin film. (b) Simulated HAADF and (d) ABF images of the non-stoichiometric grain boundary model structure which is shown in the inset. The structural units of each boundary are indicated by the polygons. A noise-reduction procedure was applied to the ABF image by a background subtraction filter [17].

repulsion between oxygen atoms changes and different translation states are stabilized. The structural units are designated by polygons. It is found that non-stoichiometric grain boundaries have nearly mirror symmetric cation arrangements with respect to the grain boundary plane, which gives better agreement with the experimental image.

The simulated HAADF and ABF images for the stable structure are shown in Fig. 2b and d, respectively. It is confirmed that the bright spots in the HAADF image correspond to Ce column locations. Weak contrast inside the structural unit, the position of which corresponds to that of oxygen in the non-stoichiometric model structure, is also visible in the HAADF image. In the case of ABF images, it is confirmed that the black and gray spots correspond to Ce and O column locations, respectively. Gray contrast due to the presence of O columns is visible inside the grain boundary structural units in the simulated ABF image, but the contrast is weaker than that for the O columns in the bulk. This is to be expected since the O column density in the grain boundary area is half that in the bulk region. It can be concluded that the non-stoichiometric grain boundary model is the most plausible model for the experimentally observed CeO_2 grain boundary and that oxygen vacancies play an important role in determining the stable grain boundary structure.

3.2 Atomic structures of $SrTiO_3$ grain boundary

Perovskite oxides, such as $SrTiO_3$ and $BaTiO_3$, exhibit a large variety of electrical properties and thus they have been utilized for electrical devices. Since some properties of the perovskite oxides arise only in polycrystalline materials, it is considered that grain boundaries play an important role for their properties. Thus, understanding the peculiar atomic structures and defect energetics at the interface is indispensable for further developments and applications of perovskite oxides. In this section, $SrTiO_3$ is selected as a model sample and the [001](310)Σ5 and [001](210)Σ5 grain boundaries are investigated by high-resolution HAADF-STEM to find the relationships among the atomic arrangements, electronic structures and defect energetics. To investigate the relationships quantitatively, the first-principles projector augmented wave method was again used [20]. In this case, three-dimensional rigid-body translation of one grain with respect to the other was taken into account to obtain the stable grain boundary structure. After obtaining the stable structure, the vacancy formation energy at possible sites in the vicinity of the grain boundary was systematically calculated.

Figure 3 shows (a) the HAADF–STEM image, (b) most stable atomic arrangements, (c) strains and (d) defect energetics of the $SrTiO_3$ [001](310)Σ5 grain boundary [21]. In the calculation, the rigid-

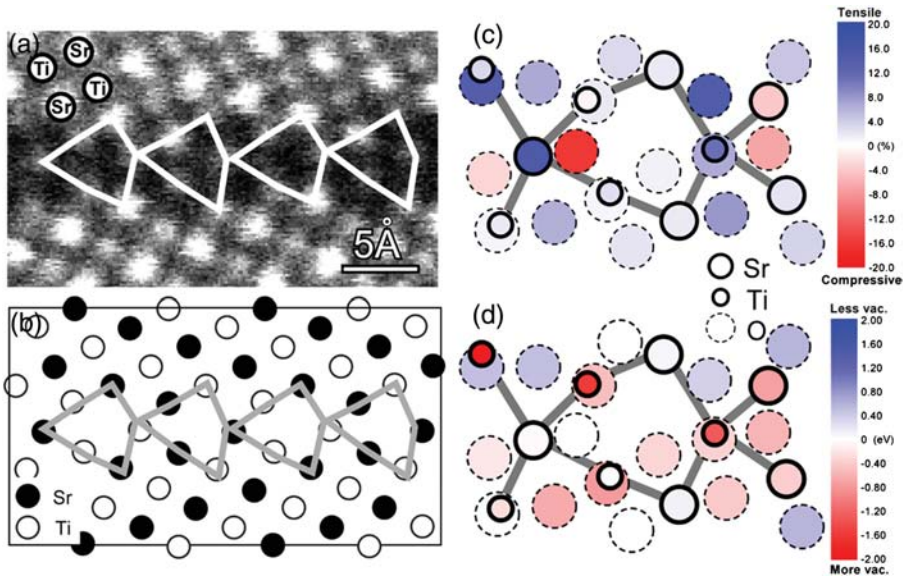

Fig. 3. (a) HAADF-STEM image, (b) calculated most stable structure, (c) strains and (d) defect energetics of $SrTiO_3$ [001](310)Σ5 grain boundary. Only Sr and Ti columns are shown in (b) to compare the theoretically obtained structure with the experimental results [21].

body translations of one grain with respect to the other were fully considered. It is seen that the calculated, most stable structure well reproduces the experimental image (Fig. 3a and b). By analyzing the calculated structure, it was found that the structural distortions, strains and dangling bonds are present mainly at the grain boundary core (Fig. 3c). On the other hand, although the vacancy formation energy depends on the atomic site, the defect energetics at the grain boundary was found to be similar to that in the bulk. It was also found that the Ti vacancy is more sensitive to structural distortions than Sr and O vacancies (Fig. 3d). This would be caused by the difference in the bonding character of Ti–O and Sr–O. On the other hand, Fig. 4 shows (a) the most stable calculated structure and (b) the HAADF–STEM image of [001](210)Σ5 grain boundary. The calculated atomic positions of the Sr and Ti–O columns of the [001](210)Σ5 grain boundary are shown as white circles in the figure. As can be seen, the shape of the structural unit formed on this grain boundary (GB) is different from that in [001](310)Σ5 grain boundary, indicating that the shape of the structural unit is influenced by the grain boundary plane although the relative orientation is the same. Through this study, the atomic structures of the Σ5 grain boundaries of $SrTiO_3$ can be fully determined, and the characteristic electronic structures and defect energetics of those grain boundaries can be identified [21].

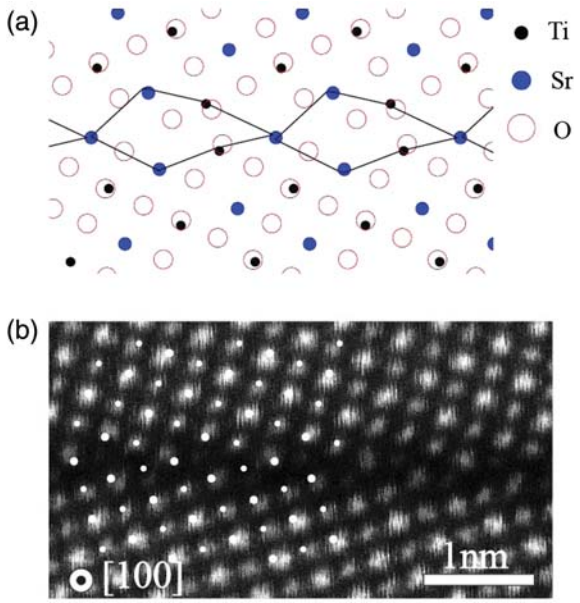

Fig. 4. (a) Most stable atomic structures of $SrTiO_3$ [001](210) Σ5 grain boundary obtained by theoretical calculation and (b) the corresponding HAADF-STEM image.

4. Grain boundary segregation

4.1 Grain boundary of Y-doped alumina ceramics

α-Alumina (Al_2O_3) is one of the most important structural ceramics for high-temperature applications and, in particular, its creep behavior has extensively been studied so far. It has been known that a small amount of lanthanide ions is effective in improving the creep behavior of Al_2O_3 ceramics [22–25]. Lanthanide ions have larger ionic radii than Al ions and tend to segregate at the grain boundaries, which are considered to retard the grain boundary sliding during creep. A number of mechanisms on the lanthanide-dopant effect have been proposed so far. It is thought that the dopants improving Al_2O_3 creep behavior affect the structure and chemistry of grain boundaries in Al_2O_3, but the mechanism of the dopant effect in Al_2O_3 has not been clarified yet in detail. In order to clarify the dopant mechanism, grain boundary atomic structures including the dopant should directly be observed for well-defined specimens. For this purpose, bicrystals are advantageous to directly study the dopant effects. This is because grain boundary characters in bicrystals can be controlled [26,27], and their atomic structures can systematically be analyzed in combination with STEM.

In this section, the atomistic mechanism of Y-doping is described, using the HAADF-STEM technique to determine the GB structure on a bicrystal pair [28,29]. The HAADF-STEM technique is especially well suited for understanding the role of heavy impurities such as Y in a bicrystal composed of much lighter ions, such as Al and O. Figure 5a shows an HAADF-STEM image of an undoped Σ31 grain boundary in Al_2O_3 [29]. Bright spots in the image correspond to atomic columns of Al (columns of oxygen do not scatter strongly enough to be seen in the image). The schematic overlay (Fig. 5b) clearly illustrates the presence of periodic structural units along the boundary plane. A notable feature of the grain boundary structure is the presence of a seven-membered ring of Al ions leading to a large open structure. Buban *et al.* [29]

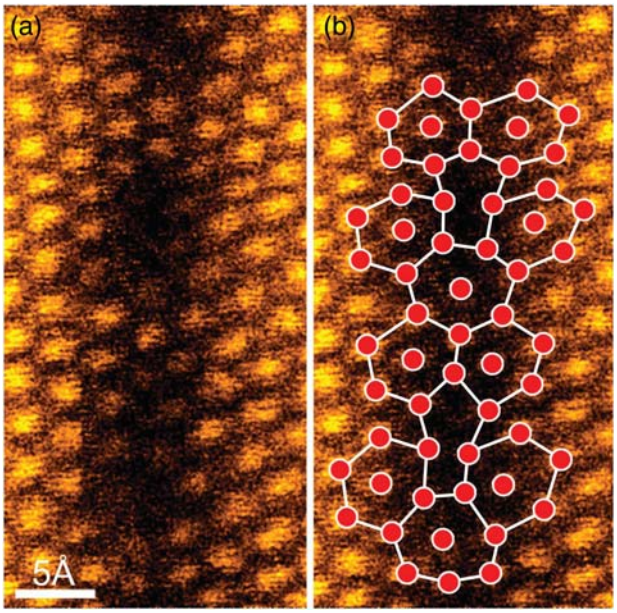

Fig. 5. (a) HAADF-STEM image of a pristine Σ31 [0001] tilt grain boundary in alumina. (b) Same image with overlay to illustrate the aluminum atomic column arrangement in the structural units. Note the large open structure of the seven-membered ring unit, which is nearly periodic along the grain boundary [29].

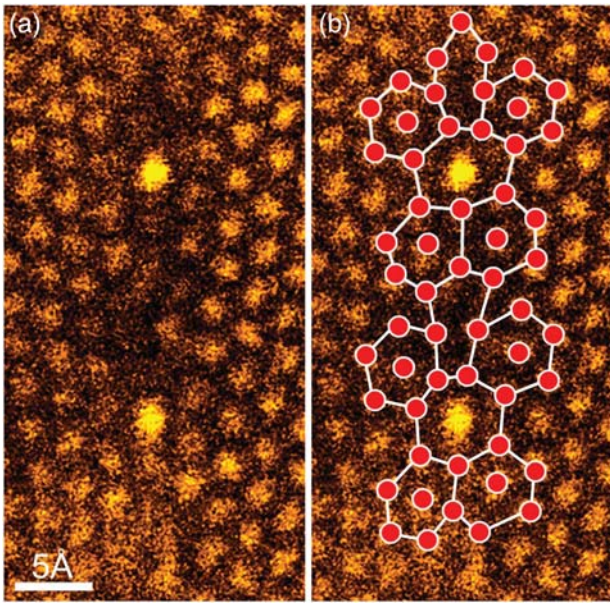

Fig. 6. (a) HAADF-STEM image of the Y-doped Σ31 [0001] tilt grain boundary in alumina. (b) Same image with overlay to illustrate the atomic column arrangement. The two brightest columns indicate the presence of the heavy Y ions. These Y containing columns are found right at the center of the seven-membered ring unit [29].

characterized Y-doped Σ31 grain boundary and showed the *Z*-contrast image shown in Fig. 6a [29]. The most striking feature is the unusually bright columns that lie periodically along the boundary plane, indicating the presence of Y. Using nanoprobe energy-dispersive spectroscopy in the STEM, Y was confirmed to be confined to the boundary plane, which is in consistent with the direct observation. Figure 6b shows a structural schematic of the Y-doped Al_2O_3 grain boundary superimposed on the image. Here, the structural units observed at the Y-doped boundary closely resemble the units found in the undoped case, suggesting that Y does not alter the basic grain boundary structure on length scales of more than ~0.1 nm. Instead, it appears that Y^{3+} simply replaces Al^{3+} on the specific site of the cation sublattice. The Y-containing columns are found at the center of the seven-membered ring, periodically along the grain boundary. Y was only rarely detected at other sites, suggesting that Y preferentially segregates to cation sites in the center of the seven-membered ring.

In order to understand the chemical and bonding environment at the grain boundary, *ab initio* calculations can provide accurate information on the local atomic bonding and charge distributions [20]. A large periodic supercell with 700 atoms containing two oppositely oriented grain boundaries was constructed using the structure obtained from static calculations. First, the supercell was constructed based on the experimentally obtained structure and fully relaxed to obtain the most accurate grain boundary structure for the undoped case. The results showed that further relaxations occurred. However, these relaxations were relatively small (<0.1 nm), yielding a grain boundary structure that still matched the structure observed in the STEM image. Next, assuming that all four distinct Al sites were substituted with Y ions in the column at the center of the seven-membered ring – the location that was observed in the STEM image – the structure was fully relaxed and, again, the final structure matched well with the corresponding experimental image.

Changes in the bonding character between the Y–O and the Al–O bonds can be best illustrated by plotting the charge density maps. Figure 7a and b shows charge density maps along the (0001)-plane for the undoped case and Y-doped case, respectively [29]. Due to the complexity of the grain boundary structure in Al_2O_3, cations and anions do not lie on the same (0001)-plane. Therefore, we have

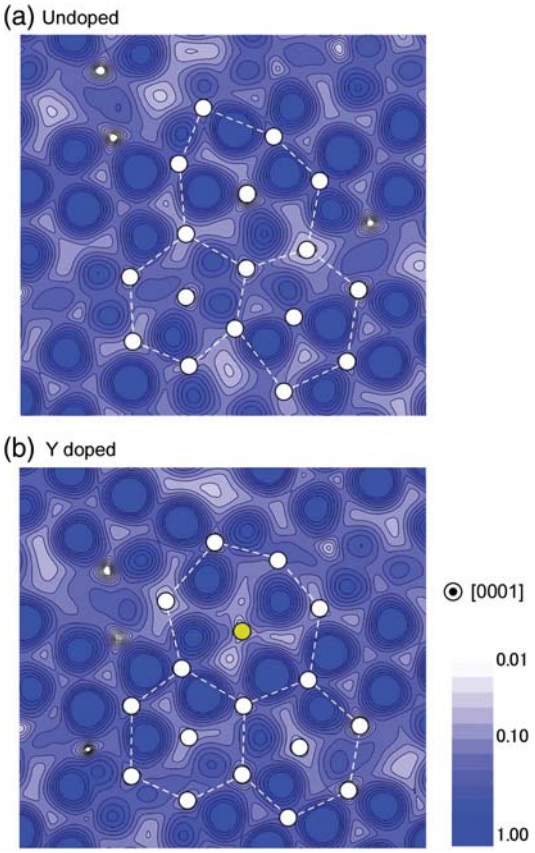

Fig. 7. A charge density map for the undoped grain boundary (a) is shown for a (0001)-plane near an Al ion in the middle of the seven-membered ring, where the charge density from the neighboring O ions (appearing as graduated blue spots) can easily be seen. A charge density map for the Y-doped grain boundary (b) is displayed using a similar (0001)-plane. Here, one can see the elongation of the O charge density toward the Y ion in the center of the seven-membered ring indicating covalent-type bonding. Note: White circles indicate the location of Al ions, while the yellow circle indicates the location of the Y column [29].

carefully selected appropriate (0001)-planes, which are close to a cation belonging to the center column of the seven-membered ring such that the charge densities of the neighboring oxygen ions can also be clearly seen. To facilitate visualization, the locations of the cation columns are indicated schematically. The charge density map for the undoped grain boundary (Fig. 7a) shows the presence of sharp nodes between the oxygen charge densities and the charge density from the Al ion in the center of the seven-membered ring. In contrast, the Y-doped grain boundary charge density map (Fig. 7b) shows that the oxygen electron densities are elongated toward the Y ion, indicating a stronger covalency for the Y–O bonds. It can be seen that Y at the center column interacts considerably with the surrounding oxygen ions. This should result in a much stronger grain boundary, which explains why the Y-doped grain boundaries can have such a large increase to creep resistance despite the fact that only a small amount of Y is present.

4.2 Grain boundary of Pr-doped ZnO varistors

It is known that zinc oxide (ZnO) ceramics show highly non-linear current–voltage characteristics. Due to these electrical properties, ZnO ceramics are used as varistors in electronic devices [30]. Doping of praseodymium (Pr) or bismuth in ZnO ceramics is a well-known method to obtain high nonlinearity in current–voltage characteristics, and the presence of the dopants at ZnO grain boundaries is thought to be an important point [31,32]. In order to understand the microscopic origin of the properties, the detailed structure of ZnO grain boundaries including the location and distribution of dopants should be known on the atomic scale. Sato *et al.* [32,33] reported the results obtained for the atomic arrangement and location of Pr at ZnO grain boundaries [32]. Grain boundaries with properly controlled orientation relationships and boundary planes were fabricated within ZnO bicrystals, thereby direct observations of the atomic arrangements were enabled. HAADF-STEM was used for the grain boundary observations.

Figure 8 shows the HAADF-STEM images of a Pr-doped ZnO grain boundary. For this grain boundary, the á0001ñ axes of both crystals are parallel to each other and the rotation angle is ~21.8° about the $\langle 1\bar{1}00\rangle$ axis to give an orientation relationship with a value of Σ7. The boundary plane is parallel to the $\{12\bar{3}0\}$-plane of both crystals. This selection of the orientation relationship and the boundary plane yields a short structural periodicity and common low-index axis for both crystals, which are well suited for atomic-resolution electron microscopic observations and calculations of atomic arrangement that are often performed under three-dimensional periodic boundary conditions. The incident electron is parallel to the [0001] axes of both crystals in the HAADF-STEM images. Therefore, Zn and O are aligned in the same columns and the position of the columns appears as bright spots. Their location was clearly observed not only in the bulk

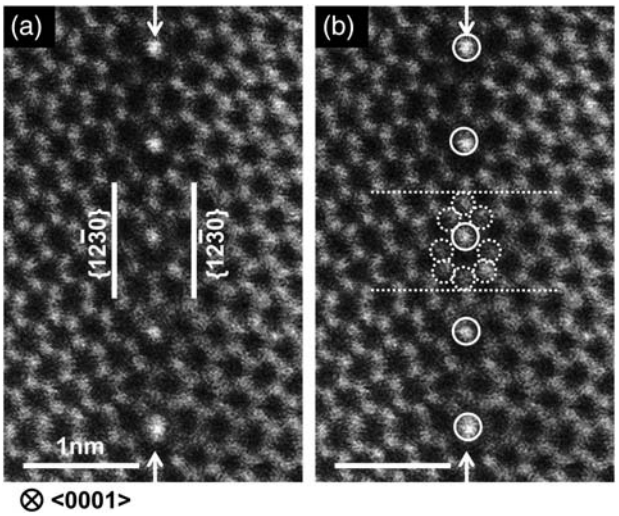

Fig. 8. (a) The HAADF-STEM image of the Pr-doped ZnO [0001] Σ7 tilt grain boundary. Electron incident direction is parallel to the ⟨0001⟩ axes of the ZnO crystals, and boundary planes are parallel to {12$\bar{3}$0}-planes. (b) The same image with an overlay of a structural unit shown by a set of circles. Arrows and dotted lines indicate the grain boundary planes and the structural periodicity along the boundary plane. Solid circles indicate positions of much higher intensities suggesting the presence of Pr at these columns [32].

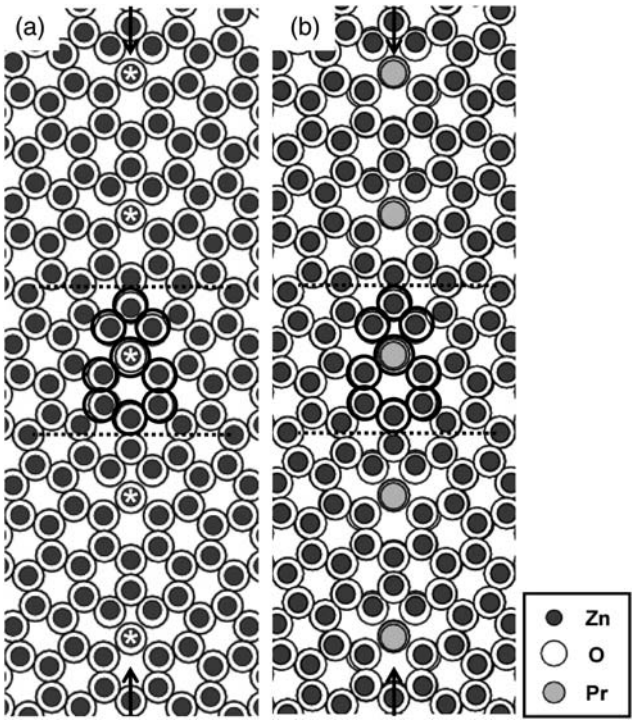

Fig. 9. Optimized atomic arrangements of (a) the undoped and (b) the Pr-doped ZnO [0001] Σ7 tilt grain boundaries. Both of the arrangements are viewed along <0001> directions. Asterisks in (a) indicate the location of atomic columns corresponding to higher intensities in STEM images (Fig. 8).

crystal, but also at the grain boundary. It was found that two ZnO crystals are directly bonded at the atomic scale at the grain boundary. This grain boundary has a structural periodicity as noted above, which is indicated by dotted lines. The atomic arrangement within one period, the structural unit, can be understood with the set of circles shown in Fig. 8b. In addition, the intensities at some particular columns are higher than those in the bulk crystal, showing the presence of heavier elements at these columns, as shown by solid circles in Fig. 8b. Since Pr has a higher atomic number ($Z = 59$) than Zn does ($Z = 30$), the higher intensities show the presence of Pr at these columns. Pr atoms preferentially occupy specific columns in the structural units and periodically appear along the boundary plane. The preference location of Pr will be discussed later. It was found that the structural unit of the Pr-doped ZnO grain boundary (sets of circles in Fig. 8b) is similar to that of the undoped ZnO boundary (sets of circles in Fig. 9a) [32,34]. This suggests that the atomic arrangement of the ZnO Σ7 tilt GB did not change significantly with the doping of Pr, and Pr simply substitutes for Zn at these columns in the structural units.

In order to obtain further insights, the stable atomic arrangement of the Pr-doped ZnO grain boundary was simulated by first-principles band-structure methods [20]. For the simulation of the Pr-doped ZnO boundary, Zn marked with asterisks was replaced with Pr, and atomic arrangements were optimized. Figure 9b shows the optimized atomic arrangement of the Pr-doped ZnO grain boundary. The atomic arrangement did not change significantly during the structural optimization, keeping the structural unit similar. The optimized atomic arrangement agrees with the HAADF-STEM image in Fig. 8, supporting the validity of the atomic arrangement in Fig. 9b from both of the experimental and theoretical sides. On this structural basis, formation energies of acceptor-like point defects such as V_{Zn} and O_i at ZnO grain boundaries were calculated [32]. It was found that the formation energies of these defects were lower for the Pr-doped case and thus, it was suggested that facilitation of defect formation is the key role of Pr-doping for the generation of non-linear current–voltage characteristics [32].

It has also been reported that Pr is selectively segregated at the sites with the longest interatomic distance [32,33]. Detailed inspection of the Pr-doped ZnO grain boundary revealed that Pr–O bonds tend to have coordination and electronic structures more similar to those in Pr_2O_3 crystal bulk, when compared with Pr–O bonds in Pr-doped ZnO bulk [33]. This would be another important insight for the reason why Pr prefers specific Zn sites in the grain boundaries. Figure 10 shows the HAADF-STEM image of the Pr-doped ZnO [0001] Σ49 GB with the incident electron beam parallel to the [0001] axes for both crystals, in which the GB atomic arrangement and the locations of Pr were clearly observed. It was found that one and two atomic columns including Pr appeared alternatively and periodically along the boundary, suggesting that there is selectivity on atomic-level locations of the Pr. This configuration is consistent with the theoretically obtained for the sites with locally longest interatomic distance, in which Pr–O bonds have similar coordination and electronic structures of Pr_2O_3.

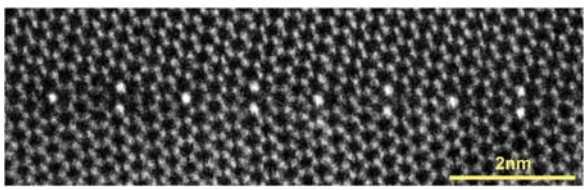

Fig. 10. The HAADF-STEM image of a Pr-doped ZnO [0001] Σ49 grain boundary. The image is observed along the [0001] common axis for both crystals [33].

4.3 Three-dimensional observation of the grain boundary of Y-doped Al_2O_3

As shown in Sections 4.1 and 4.2, HAADF-STEM is well suited to identifying heavy elements at grain boundaries. However, the most direct approach is to observe the specimen from multiple directions, such as cross-sectional and plan-view directions, provided the different images can be interpreted equally well. Shibata *et al.* [35] first demonstrated that the aberration-corrected HAADF-STEM is a powerful method to directly highlight individual dopant atoms on buried crystalline interfaces. As a model system, a Y-doped α-Al_2O_3 grain boundary was prepared by diffusion bonding of two single crystals in the Σ13 orientation relationship [36,37]. Y was added to the interface before diffusion bonding, as described elsewhere [28,37]. Figure 11a shows schematically the bicrystal fabricated in this study. The bicrystallography of the interface between the top and bottom crystals is summarized as follows: $[1\bar{2}10]_{top}||[\bar{1}2\bar{1}0]_{bottom}$, $[1\bar{2}10]_{top}||[\bar{1}2\bar{1}0]_{bottom}$ and $[\bar{2}021]_{top}||[\bar{2}021]_{bottom}$ [35,37]. The interface normal is parallel to the high-index $\langle 50\bar{5}4\rangle$ directions in both the top and bottom crystals. Figure 11b shows typical atomic-resolution HAADF-STEM images of the interface projected along the $\langle 1\bar{2}10\rangle$ and $\langle \bar{2}021\rangle$ directions. The doped Y atomic columns are clearly imaged with very strong contrast along the boundary

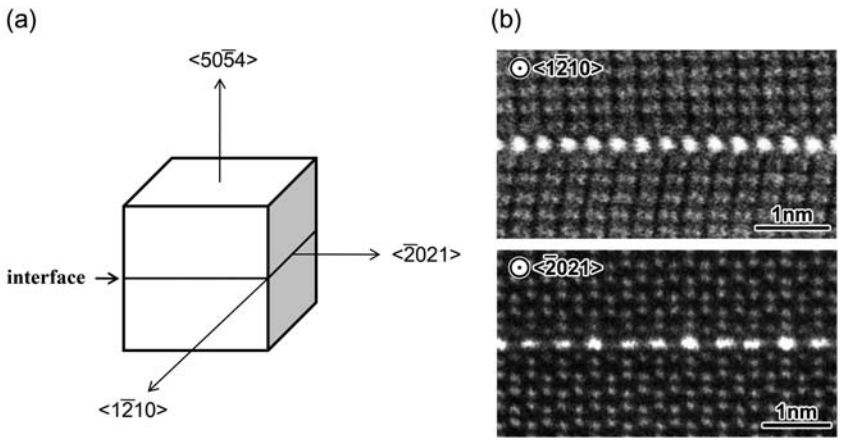

Fig. 11. Schematic illustration and two cross-sectional HAADF-STEM images of the Y-doped Σ13 grain boundary of α-Al_2O_3. (a) Schematic illustration of the α-Al_2O_3 bicrystal fabricated in this study, with the orientation relationship between the top and bottom crystals, is indicated. Y atoms are artificially doped in the boundary plane. (b) HAADF-STEM images of the Y-doped grain boundary observed from two orthogonal directions parallel to the interface plane [35].

and form a monoatomic layer structure in the core of the boundary.

Figure 12 shows three HAADF-STEM images of the Y-doped Σ13 grain boundary observed from three directions [35]. The plan-view image is the fast Fourier transform (FFT)-filtered image and is observed from the ⟨50$\bar{5}$4⟩-direction perpendicular to the interface plane. In this plan-view image, the interface Y atoms are visible as strong image intensity spots due to their much larger atomic number compared with Al and O atoms. These spots are periodically arrayed along the ⟨$\bar{2}$021⟩-direction. In addition, there are some clear deviations of the Y atom positioning from the ordered positions. It was sometimes seen that Y atoms were shifted in between the ordered array sites, as indicated by the arrows. The present results thus demonstrate that Y positioning at the grain boundary is basically ordered in two dimensions based on their specific stable atom positions on the interface, but that some fluctuation or disordering exists, perhaps due to trapping and/or overflowing onto metastable sites. The two cross-sectional images shown in Fig. 11b could not detect these stray Y atoms because of their very low density along the projected directions. Thus, plan-view HAADF-STEM can be a very powerful method for directly imaging individual atoms within materials, bringing us a crucial step toward the full three-dimensional characterization of interface atomic structures.

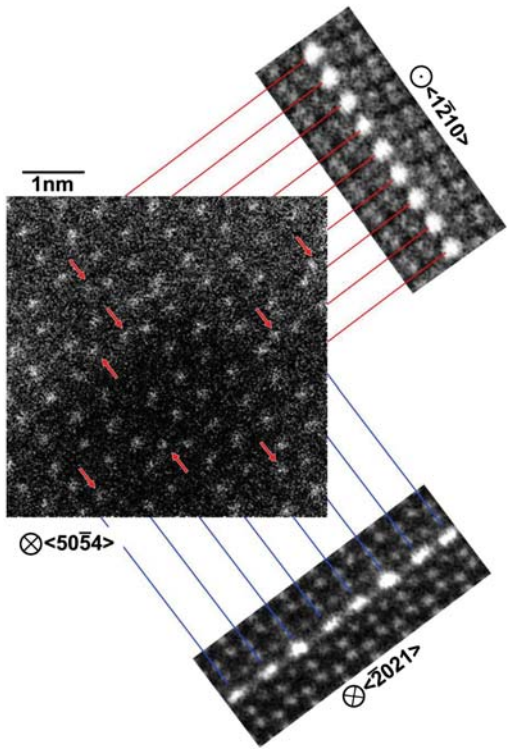

Fig. 12. Plan-view and two cross-sectional HAADF-STEM images obtained for Σ13 grain boundary of α-Al_2O_3, which clearly show the two-dimensional positioning of the individual Y atoms on the interface. The plan-view image was obtained by a simple FFT-masking method to remove the background stripes from the original image. The image is displayed with a nonlinear intensity scale to highlight bright features [35].

5. Direct observation of light elements

5.1 Oxygen vacancy ordering in $LiMn_2O_4$

Lithium manganese oxide spinel ($LiMn_2O_4$) has the cubic spinel structure (space group $Fd\bar{3}m$) with a lattice parameter of $a = 8.2449$ Å at room temperature [38]. In stoichiometric $LiMn_2O_4$, half the manganese exists as Mn^{3+} and the other half as Mn^{4+}, with the ions distributed randomly throughout the crystal at room or higher temperatures. A phase transition has been observed slightly below room temperature from cubic to orthorhombic symmetry due to charge ordering of Mn^{3+} and Mn^{4+} ions as a result of the co-operative interactions between Jahn–Teller-distorted Mn^{3+} ions on the octahedral site [39]. The presence of oxygen vacancies introduced by altering the synthesis conditions and starting reagents [40] leads to a tetragonal spinel phase (space group $I4_1/amd$) $LiMn_2O_{4-\delta}$ above room temperature [41]. The detailed local structures of O and Mn are critical in understanding the electrochemical processes occurring during the battery use.

Figure 13a shows an HAADF-STEM image of a typical $LiMn_2O_4$ particle synthesized by pyrolysis in O_2 at 700°C of a precursor powder prepared by ligand exchange of lithium isopropoxide and manganese ethoxide with 2-ethoxyethanol [12,42]. To obtain detailed information of Li and O distribution, electron energy loss spectroscopy (EELS) analyses for the center and surface regions of the $LiMn_2O_4$ particle were carried out [12]. Figure 13b shows the Mn-$M_{2,3}$ and Li-K energy-loss near-edge fine structure (ELNES) for center and near-surface regions after background subtraction, normalized to the intensity of the Mn-$M_{2,3}$ edge. A higher Li concentration in the center region than the surface region is apparent. In Fig. 13c, the Mn-$L_{2,3}$ peak for the subsurface region is

seen to shift to the low-energy side compared with the center region, which is consistent with the observed chemical shift of Mn-$M_{2,3}$ in Fig. 13b. This indicates that the valence of Mn in the subsurface region is less than in the center region. Quantitative analysis of the EELS spectra reveals that the Mn/O ratios increase from 0.50 ± 0.07 in the center region to 0.68 ± 0.09 in the surface region. A tetragonal lithium manganese spinel structure can thus be inferred to exist in the surface region with O and Li deficiency, which is an intrinsic feature of nanocrystalline $LiMn_2O_4$ [12].

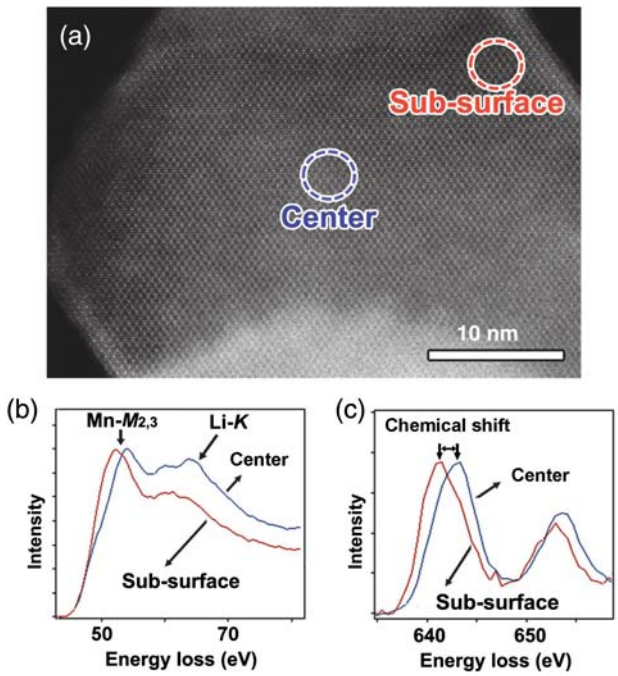

Fig. 13. (a) STEM image of a typical $LiMn_2O_4$ particle. The areas for EELS analysis were marked with dashed cycles. (b) ELNES of Mn-$M_{2,3}$ and Li-K showing the difference in Li concentration between the center and surface regions, as well as the chemical shift of Mn-$M_{2,3}$. (c) ELNES of the Mn-$L_{2,3}$ edge showing a chemical shift from the center to the surface region [12].

Tetragonal (oxygen-deficient) lithium manganese spinel has lattice constants $a = b = 5.7356$ Å and $c = 8.6464$ Å [40], which corresponds to pseudo-cubic lattice parameters $a_c = b_c = 8.1114$ Å and $c_c = 8.6464$ Å. The diamonds demarcated by Mn columns along the $\langle 110 \rangle_{cubic}$ zone axis group are degenerated into $[100]_{tetragonal}$, $[010]_{tetragonal}$ and $[111]_{tetragonal}$ zone axes. The short and long diagonals of the Mn diamond viewed along $[100]_{tetragonal}$ are 5.7356 and 8.6464 Å, respectively, giving a ratio of 0.663, which is smaller than 0.707 for the cubic spinel structure. In contrast, the short and long diagonals of the Mn diamond viewed down the $[111]_{tetragonal}$ zone axis are 5.9278 and 8.1114 Å, respectively, giving a ratio of 0.731. Thus, measurement of the ratio of the projected distance along the short diagonal to the distance along the long diagonal can be used to distinguish between the tetragonal phase and cubic phase in lithium manganese spinel. Huang *et al.* [12] observed the HAADF-STEM image of the subsurface region of the small $LiMn_2O_4$ particle along the $[110]_{cubic}$ zone axis. The image is shown in Fig. 14a, which was obtained at the detection angle (β) of 92–228 mrad. The Mn diamond arrangement is clearly seen, with brighter contrast corresponding to the Mn-1 columns and lesser contrast to the Mn-2 columns, consistent with the difference in atomic density along these two Mn sites. No contrast from O or Li sites can be discerned. The ratio of the short and long diagonals of the Mn diamond, measured from the raw HAADF-STEM image, is $m/n = 0.667$.

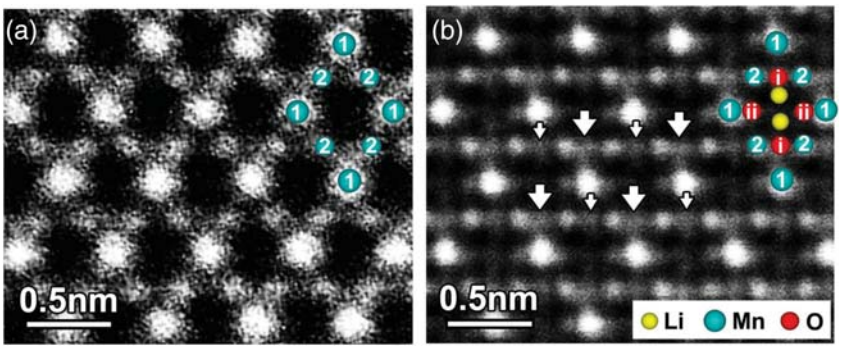

Fig. 14. ADF images of a tetragonal $Li_{1-x}Mn_2O_{4-\delta}$ particle along the $[100]_{tetragonal}$ zone axis. (a) Detection angle of 92–228 mrad showing the diamond configuration of Mn columns. The Mn-1 and Mn-2 sites have different contrast levels. (b) Detection angle of 52–140 mrad revealing alternating oxygen contrast levels (large and small arrows) and the shift in O-i columns. The structure model is superposed on the image [12].

This indicates that the crystal has the tetragonal structure, consistent with the measured oxygen deficiency and expected Jahn–Teller distortion from the EELS analysis.

To enhance the contrast for light elements, a small detection angle was used. Figure 14b shows an ADF-STEM image of the subsurface region of an $Li_{1-x}Mn_2O_{4-\delta}$ particle along a $[100]_{tetragonal}$ zone axis obtained with a detection angle of 52–140 mrad [12]. The diamond arrangement of bright Mn-1 columns and darker Mn-2 columns, similar to the HAADF-STEM image in Fig. 14a, is clearly visible. The O columns also have sufficient contrast to be discernable [12]. Interestingly, the intensity of O-i columns is not uniform, exhibiting alternately brighter and darker contrast, as highlighted by the large and small arrows in Fig. 14b. This indicates the presence of vacancies in the dark O-i columns, consistent with the lack of O in the surface region detected by EELS [12]. In addition, O-ii columns show weaker contrast than the brighter O-i columns due to the delocalization caused by the misalignment of oxygen atoms; these appear as shoulders of Mn-1 site signals because the strong Mn-1 contrast dominates over the weaker contrast of oxygen. These structural and compositional information are useful for understanding the charge/discharge behavior and capacity fade in lithium ion batteries with $LiMn_2O_4$ as the cathode material.

During observation of light elements in ceramics, electron irradiation damage often takes place. This is because STEM utilizes a focused electron beam and the ceramic materials with included lithium and hydrogen are usually sensitive to the electron irradiation. To avoid the damage, the samples were observed by a relatively weak electron beam current <35 pA. In this case, the pixel dwell time was ~32 μs per pixel, and the typical electron dose was roughly in the magnitude of $\sim 2.8 \times 10^5$ e^- $Å^{-2}$. In addition, relatively thick areas were observed in a very short time, and the measurements were taken for a number of sample areas and even from several TEM samples. Based on these careful experiments, the electron beam damage was able to be minimized, and the reproducible results were obtained.

5.2 Direct observation of Li ions by ABF imaging

Huang *et al.* [12,13] applied the ABF-STEM technique to directly observe Li ions in the lithium battery crystals. Figure 15a shows an ABF image of the subsurface region of an $LiMn_2O_{4-\delta}$ particle viewed along [100], using a detection angle of 6–25 mrad. The Li ions are clearly visible together with the O and Mn columns in the ABF image, as indicated by the atomic structure overlaid in the figure. They slightly shift away from their original positions as described above due to the presence of O vacancies. The image simulation unambiguously reproduces the image contrast in the experimental ABF image [12]. Figure 15b shows a typical ABF image obtained from the $LiCoO_2$ thin-film viewed

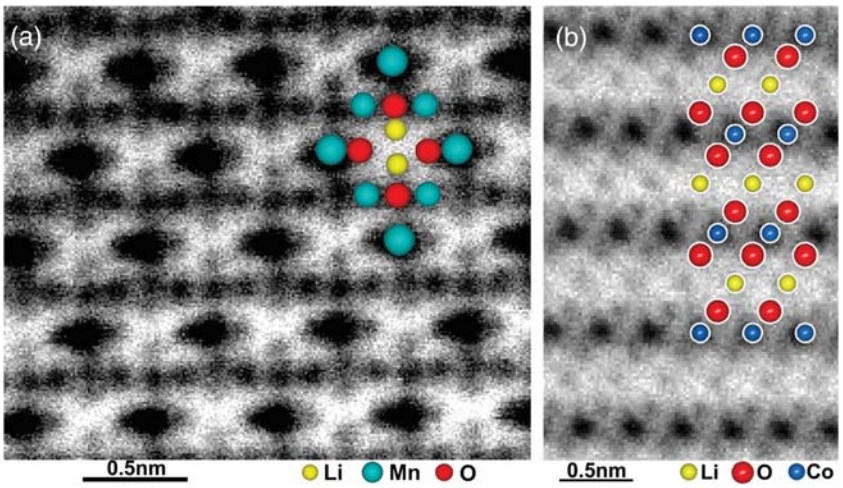

Fig. 15. (a) ABF images of tetragonal $LiMn_2O_{4-\delta}$ spinel nanoparticles along zone axis [100] [12]. (b) A typical ABF image of an $LiCoO_2$ thin film viewed along the $[\bar{1}\bar{1}20]$ zone axis with the Li columns clearly visible [13]. Both of the crystal structure models are superposed.

along [$\overline{1}$120] [13]. Li sites as well as O and Co sites are clearly visible, which can be distinguished according to the image contrast, as illustrated by the atomic structure model inset in the figure, and confirmed by the ABF image simulation [13]. These two examples demonstrate that ABF imaging in Cs-corrected STEM is a reliable technique for directly observing light elements in this category of material. Further, the Li sites are observed directly, in real time, without any further image processing; this is an important distinction compared with traditional high-resolution TEM techniques [43].

In the case of high-resolution TEM, the image contrast is very sensitive to sample thickness and defocus value, and interpretation of the images is not intuitive, usually requiring complex image simulations and greater operational expertise. In contrast, the ABF image in a Cs-corrected STEM provides consistent image contrast over a large range of sample thickness. Also, altering the defocus value simply washes out the image, which helps to determine the right defocus condition in the experiment [11]. Thus, ABF images of systems containing both light and heavy elements can be interpreted more intuitively and robustly. ABF can thus be said to be a useful method for analyzing light elements such as Li.

5.3 Direct observation of hydrogen columns by ABF imaging

Directly imaging hydrogen is more difficult than lithium, though Meyer *et al.* [44] have suggested that the sensitivity required to image individual hydrogen atoms absorbed onto a grapheme sheet is achievable. Since direct visualization of lithium has been accomplished with the use of ABF-STEM imaging, it is natural to challenge the atomic resolution imaging of hydrogen columns in a crystalline environment, which is the lightest element.

VH_2 has an fcc V sublattice with a lattice constant of 0.427 nm. Viewed along the [001] zone axis, and the interatomic spacing between hydrogen atoms along-axis is 0.21 nm, while the projected distance between the H columns and their nearest-neighbor V columns is 0.15 nm. Smaller interatomic spacings along the column of interest, but larger separations between adjacent columns, favor ABF–STEM imaging. Figure 16a shows the ADF image of VH_2 viewed along the [001] zone axis [15]. The projected model structure is superposed in the figure. The signal in ADF STEM is known to scale approximately as the square of the atomic number. Hydrogen, $Z = 1$, is thus invisible in this image; whatever contribution it offers is completely dominated by the signal from the vanadium, $Z = 23$, columns. The simultaneously acquired ABF raw image is shown in Fig. 16b. The inset of the figure is a simulated ABF image assuming a specimen thickness of 5 nm. The agreement is fairly good. Although with weaker contrast than the vanadium columns, there is a perceptible dip in the signal at the expected location of the hydrogen columns in VH_2 which is supported by ABF image simulations [15]. Thus, the full elemental observation and analyses come into the truth in an STEM and might have strong impact on the battery-related research field.

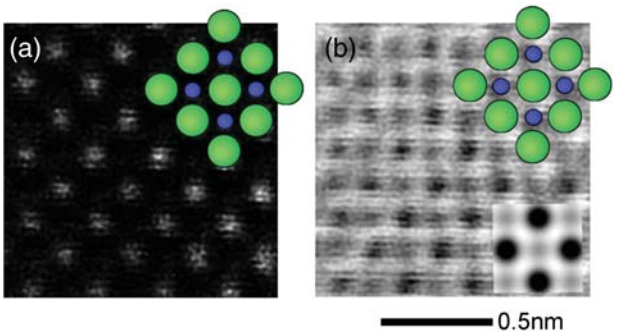

Fig. 16. (a) ADF image of a crystal of VH_2 viewed along [001]. (b) The ABF image recorded simultaneously with (a). The projected structure is superposed on all images. A simulated ABF image assuming a specimen thickness of 5 nm is superposed on (b) [15].

6. Conclusions

Aberration-corrected STEM, allowing the formation of sub-angstrom-sized electron probes, is capable of finding grain boundaries and light elements present in a crystal. HAADF imaging provides directly and robustly interpretable structural images with clear atomic number (Z) contrast and is thus eminently suited to problems where direct visualization of the local atom structure is desired. Direct imaging by HAADF-STEM will assist the characterization of the complex crystal structures such as ceramic grain boundaries. It has enabled the probing of individual dopant atoms and the structure of grain boundaries. It can further be used in conjunction with

techniques such as EELS for investigating chemical composition and electrical structure, and the emerging technique of ABF imaging for direct visualization of light atoms. The greatest advantage of the STEM technique is its ability to record multiple signals simultaneously. The ability to probe the atomic-scale structural and electronic properties in precise correlation constitutes a powerful tool for revealing the connection between form and function that is the goal of much materials' science analysis. We foresee that atomic-resolution STEM will continue to have much to offer nano-scale materials science well into the future.

In this review, the atomic structure determination of CSL grain boundaries and direct observation of grain boundary-segregated dopants and light elements in ceramics were shown to combine with the theoretical calculations. It was demonstrated that the combination of STEM characterization and first-principles calculation are very useful to interpret the structural information and to understand the origin of the properties in various ceramics. Such characterizations were, until a couple of years ago, practically impossible to carry out, but recent development of Cs-corrected STEM enables us to directly characterize single atoms in solid and light elements such as lithium and hydrogen. This breakthrough will make it possible to apply many materials' properties which have not been still clarified from the atomic scale. We therefore find ourselves entering a new stage of the research for the rational design and development of new materials science.

Acknowledgement

The author acknowledges N. Shibata, S.D. Findlay, H. Hojo, T. Tohei, T. Mizoguchi, J. Buban, H.-S. Lee, Y. Sato, T. Yamamoto, R. Huang, H. Moriwake, Y.H. Ikuhara, A. Kuwabara, T. Saito, C.A.J. Fisher, T. Hitosugi, H. Oki, J. Matsuda, E. Akiba and T. Hirayama.

Funding

This work was supported by the Grants-in-Aid for Scientific Research on Priority Areas 'Nano Materials Science for Atomic-scale Modification' (No. 19053001) from the Ministry of Education, Culture, Sports, Science and Technology (MEXT) and also by Japan Society for the Promotion of Science (JSPS) through its 'Funding Program for World-Leading Innovative R&D on Science and Technology (FIRST Program)'.

References

1 Sutton A P and Ballufi R W (1995) *Interfaces in Crystalline Materials* (Oxford University Press, USA).

2 Sakuma T, Shepard L, and Ikuhara Y (eds) (2000) *Grain Boundary Engineering in Ceramics: From Grain Boundary Phenomena to Grain Boundary Quantum Structures*. Ceramic Transactions, 118 (The American Ceramic Society, Westeville).

3 Ikuhara Y (2001) Grain boundary and interface structures in ceramics. *J. Ceram. Soc. Jpn.* **109**: S110.

4 Ikuhara Y, Yoshida H, and Sakuma T (2001) Impurity effects on grain boundary strength in structural ceramics. *Mater. Sci. Eng. A* **319–321**: 24–30.

5 Haider M, Rose H, Uhlemann S, Kabius B, and Urban K (1998) Towards 0.1 nm resolution with the first spherically corrected transmission electron microscope. *J. Electron Microsc.* **47**: 395.

6 Pennycook S J and Jesson D E (1990) High-resolution incoherent imaging of crystals. *Phys. Rev. Lett.* **64**: 938.

7 Pennycook S J and Jesson D E (1991) High-resolution *Z*-contrast imaging of crystals. *Ultramicroscopy* **37**: 14.

8 Nellist P D, Chisholm M F, Dellby N, Krivanek O L, Murfitt M F, Szilagyi Z S, Lupini A R, Borisevich A Y, Sides W H, and Pennycook S J (2004) Direct sub-angstrom imaging of a crystal lattice. *Science* **305**: 1741.

9 Okunishi E, Ishikawa I, Sawada H, Hosokawa F, Hori M, and Kondo Y (2009) Visualization of light elements at ultrahigh resolution by STEM annular bright field microscopy. Microsc. Microanal. **15** (Suppl. 2): 164.

10 Findlay S D, Shibata N, Sawada H, Okunishi E, Kondo Y, Yamamoto T, and Ikuhara Y (2009) Robust atomic resolution imaging of light elements using scanning transmission electron microscopy. *Appl. Phys. Lett.* **95**: 191–913.

11 Findlay S D, Shibata N, Sawada H, Okunishi E, Kondo Y, and Ikuhara Y (2010) Dynamics of annular bright field imaging in scanning transmission electron microscopy. *Ultramicroscopy* **110**: 903–923.

12 Huang R, Ikuhara Y H, Mizoguchi T, Findlay S D, Kuwabara A, Fisher C A J, Moriwake H, Oki H, Hirayama T, and Ikuhara Y (2011) Oxygen-vacancy ordering at surfaces of lithium manganese(III, IV) oxide spinel nanoparticles. *Angew Chem. Int. Ed.* **50**: 3053–3057. DOI:10.1002/anie.201004638.

13 Huang R, Hitosugi T, Findlay S D, Fisher C A J, Ikuhara Y H, Moriwake H, Oki H, and Ikuhara Y (2011) Real-time direct observation of Li in $LiCoO_2$ cathode material. *Appl. Phys. Lett.* **98**: 051913.

14 Oshima Y, Sawada H, Hosokawa F, Okunishi E, Kaneyama T, Kondo Y, Niitaka S, Takagi H, Tanishiro Y, and Takayanagi K (2010) Direct imaging of lithium atoms in LiV_2O_4 by spherical aberration-corrected electron microscopy. *J. Electron Microsc.* **59**: 457–461.

15 Findlay S D, Saito T, Shibata N, Sato Y, Matsuda J, Asano K, Akiba E, Hirayama T, and Ikuhara Y (2010) Direct imaging of hydrogen within a crystalline environment. *Appl. Phys. Expess.* **3**: 116603.

16 Ishikawa R, Okunishi E, Sawada H, Kondo Y, Hosokawa F, and Abe E (2011) Direct imaging of hydrogen-atom columns in a crystal by annular bright-field electron microscopy. *Nat. Mater.* **10**: 278–281. DOI:10.1038/NMAT2957.

17 Hojo H, Mizoguchi T, Ohta H, Findlay S D, Shibata N, Yamamoto T, and Ikuhara Y (2010) Atomic structure of a CeO_2 grain boundary: the role of oxygen vacancies. *Nano Lett.* **10**: 4668.

18 Gale J D and Rohl A L (2003) The general lattice utility program (GULP). Mol. Simulat. **29**: 291–341.

19 Gale J D (1997) GULP: a computer program for the symmetry-adapted simulation of solids. *J. Chem. Soc. Faraday Trans.* **93**: 629.

20 Kresse G and Furthmüller J (1996) Efficient iterative schemes for *ab initio* total-energy calculations using a plane-wave basis set. *Phys. Rev. B* **54**: 11169.

21 Imaeda M, Mizoguchi T, Sato Y, Lee H S, Findlay S D, Shibata N, Yamamoto T, and Ikuhara Y (2008) Atomic structure, electronic structure, and defect energetics in [001](310)Σ5 grain boundaries of $SrTiO_3$ and $BaTiO_3$. *Phys. Rev. B* **78**: 245320-1–245320-12.

22 Yoshida H, Ikuhara Y, and Sakuma T (1999) High-temperature creep resistance in lanthanoid ion-doped polycrystalline Al_2O_3. *Phil. Mag. Lett.* **79**: 249.

23 Yoshida H, Ikuhara Y, and Sakuma T (1998) High-temperature creep resistance in rare-earth-doped, fine-grained Al_2O_3. *J. Mater. Res.* **13**: 2597.

24 Cho J, Harmer M P, Chan M, Rickman J M, and Thompson A M (1997) Effect of yttrium and lanthanum on the tensile creep behavior of aluminum oxide. *J. Am. Ceram. Soc.* **80**: 1013.

25 Yoshida H, Ikuhara Y, and Sakuma T (2002) Grain boundary electronic structure related to the high temperature creep resistance in polycrystalline Al_2O_3. *Acta Metall.* **50**: 2955.

26 Ikuhara Y, Watanabe T, Saito T, Yoshida H, and Sakuma T (1999) Atomic structure and chemical bonding state of sapphire bicrystal. *Mater. Sci. Forum* **294**: 273.

27 Gemming T, Nufer S, Kurtz W, and Ruhle M (2003) Structure and chemistry of symmetrical tilt grain boundaries in α-Al_2O_3: I, bicrystals with "clean" interface. *J. Am. Ceram. Soc.* **86**: 581.

28 Matsunaga K, Nishimura H, Muto H, Yamamoto T, and Ikuhara Y (2003) Direct measurements of grain boundary sliding in yttrium-doped alumina bicrystals. *Appl. Phys. Lett.* **82**: 1179.

29 Buban J P, Matsunaga K, Chen J, Shibata N, Ching W Y, Yamamoto T, and Ikuhara Y (2006) Grain boundary strengthening in alumina by rare earth impurities. *Science* **311**: 212.

30 Clarke D R (1999) Varistor ceramics. *J. Am. Ceram. Soc.* **82**: 485.

31 Mukae K, Tsuda K, and Nagasawa I (1977) Non-ohmic properties of ZnO–rare earth metal oxide Co_3O_4 ceramics. *Jpn. J. Appl. Phys.* **16**: 1361.

32 Sato Y, Mizoguchi T, Shibata N, Yodogawa M, Yamamoto T, and Ikuhara Y (2006) Role of Pr segregation in acceptor-state formation at ZnO grain boundaries. *Phys. Rev. Lett.* **97**: 106802.

33 Sato Y, Mizoguchi T, Shibata N, Yamamoto T, Hirayama T, and Ikuhara Y (2009) Atomic-scale segregation behavior of Pr at a ZnO [0001] Σ49 tilt grain boundary. *Phys. Rev. B* **80**: 094114.

34 Oba F, Ohta H, Sato Y, Hosono H, Yamamoto T, and Ikuhara Y (2004) Atomic structure of [0001]-tilt grain boundaries in ZnO: a high-resolution TEM study of fiber-textured thin films. *Phys. Rev. B* **70**: 125415.

35 Shibata N, Findlay S D, Azuma S, Mizoguchi T, Yamamoto T, and Ikuhara Y (2009) Atomic-scale imaging of individual dopant atoms in a buried interface. *Nat. Mater.* **8**: 654.

36 Fabris S and Elsässer C (2001) Σ13 (101(_)4) twin in α-Al_2O_3: a model for a general grain boundary. *Phys. Rev. B* **64**: 245117.

37 Azuma S, Shibata N, Findlay S D, Mizoguchi T, Yamamoto T, and Ikuhara Y (2010) HAADF STEM observations of a Σ13 grain boundary in α-Al_2O_3 from two orthogonal directions. *Phil. Mag. Lett.* **90**: 539–546. doi:10.1080/09500831003630765.

38 Thackeray M M, David W I F, Bruce P G, and Goodenough J B (1983) Lithium insertion into manganese spinels. *Mater. Res. Bull* **18**: 461–472.

39 Rodríguez-Carvajal J, Rousse G, Masquelier C, and Hervieu M (1998) Electronic crystallization in a lithium battery material: columnar ordering of electrons and holes in the spinel $LiMn_2O_4$. *Phys. Rev. Lett.* **81**: 4660.

40 Yonemura M, Yamada A, Kobayashi H, Tabuchi M, Kamiyama T, Kawamoto Y, and Kanno R (2004) Synthesis, structure, and phase relationship in lithium manganese oxide spinel. *J. Mater. Chem.* **14**: 1948–1958.

41 Kanno R, Kondo A, Yonemura M, Gover R, Kawamoto Y, Tabuchi M, Kamiyama T, Izumi F, Masquelier C, and Rousse G (1999) The relationships between phases and structures of lithium manganese spinels. *J. Power Sources* **81–82**: 542–546.

42 Ikuhara Y H, Iwamoto U, Kikuta K, and Hirano S (1999) Synthesis, electrochemical, and microstructural study of precursor-derived $LiMn_2O_4$ powders. *J. Mater. Res.* **14**: 3102–3110.

43 Shao-Horn Y, Croguennec L, Delmas C, Nelson E C, and O'Keefe M A (2003) Atomic resolution of lithium ions in $LiCoO_2$. *Nat. Mater.* **2**: 464–467.

44 Meyer J, Girit C O, Crommie M F, and Zettl A (2008) Imaging and dynamics of light atoms and molecules on grapheme. *Nature* **454**: 319–322.